Journal of Wind Engineering & Industrial Aerodynamics 243 (2023) 105570

Contents lists available at ScienceDirect

Journal of Wind Engineering & Industrial Aerodynamics

journal homepage: www.elsevier.com/locate/jweia

Experimental translating downbursts immersed in the atmospheric boundary layer

Federico Canepa [a,b,*], Djordje Romanic [c,b], Horia Hangan [d,b], Massimiliano Burlando [a]

[a] Department of Civil, Chemical and Environmental Engineering (DICCA), Polytechnic School, University of Genoa, Via Montallegro 1, 16145, Genoa, Italy
[b] Wind Engineering, Energy and Environment (WindEEE) Research Institute, Western University, 2535 Advanced Avenue, London, Ontario, N6M 0E2, Canada
[c] Department of Atmospheric and Oceanic Sciences, Faculty of Science, McGill University, Burnside Hall, 805 Sherbrook Street West, Montreal, Quebec, H3A 0B9, Canada
[d] Faculty of Engineering and Applied Science, Ontario Tech University, 2000 Simcoe Street North, Oshawa, Ontario, L1G 0C5, Canada

ARTICLE INFO

Keywords:
Downburst
Impinging Jet
ABL
Storm motion
Turbulence
Wind simulator
Vertical profiles
Non-linearity

ABSTRACT

Thunderstorm winds are cold descending gravity currents whose impingement on the ground creates strong radial outflows with maximum wind speeds in the near-ground region. They represent one of the greatest hazards for natural and built environment as well as one of the deadliest phenomena all over the world. This study carries on the post-processing analyses of the downburst experimental campaign performed at the WindEEE Dome, at Western University in Canada, in the context of the ERC project THUNDERR. While a former study presented the interaction between downburst and atmospheric boundary layer (ABL) winds, here the focus is on the influence exerted by the thunderstorm cloud translation. This was experimentally replicated at large scale by means of impinging jet technique where the jet axis was inclined to a non-zero angle with respect to the vertical. Finally, the inclusion of background ABL wind allowed to reconstruct the complete three-dimensional and non-stationary nature of the phenomenon. The outflow radial symmetry is lost in case of inclined jet axis. This leads to an intensification of the front-wind side and weakening of the rear-wind side, where the entrainment of the counter-directed ABL wind, and consequent flow speed-up, are not as pronounced as in the vertical-axis case. The non-linearity of the complex interaction between downburst, ABL flow and cloud translation is proven and quantified. Vertical profiles of mean wind speed and turbulence intensity are discussed in relation to the mutual interaction among flow components.

1. Introduction

Thunderstorm downbursts are extreme and non-stationary wind phenomena at the meso-γ scale (2–20 km) usually associated with deep moist convection. Along with extra-tropical cyclones, they dominate the wind climate at the mid-latitudes of many parts of the world. Recent and expected future increases in frequency and severity of thunderstorms seem to correlate with ongoing climate changes over the earth planet (Allen, 2018; Rädler et al., 2019). Downbursts have spatiotemporal characteristics profoundly different from those of extra-tropical cyclones at the synoptic scale. The evaporation and melting of hydrometeors inside and underneath the cumulonimbus cloud in the subsaturated environment, as well as the drag due to the falling raindrops or ice, are the main contributors to the negative buoyancy of the air parcels that drive the downdraft to the surface. The extracted latent heat of evaporation/melting/sublimation from the ambient air results in its negative buoyancy and downward acceleration in the precipitation region. Once the downdraft hits the surface, it often creates an intense radial outflow with nose-like vertical profile of velocity (Fujita, 1981, 1985; Hjelmfelt, 1988; Lombardo et al., 2014; Solari et al., 2015; Canepa et al., 2020). In contrast to the logarithmic-like profile of atmospheric boundary layer (ABL) winds, the maximum radial velocities in downburst outflows are experienced in the near-surface region. Downbursts are spatially classified into macro-bursts and micro-bursts depending on whether the horizontal size of the outflow is greater or smaller than 4 km, respectively (Fujita, 1985). The diameter of thunderstorm downdrafts typically varies from approximately 400 m to several km (Hjelmfelt, 1988; Mason et al., 2009a; Zhang et al., 2013).

* Corresponding author. Department of Civil, Chemical and Environmental Engineering (DICCA), Polytechnic School, University of Genoa, Via Montallegro 1, 16145, Genoa, Italy.
E-mail address: federico.canepa@edu.unige.it (F. Canepa).

https://doi.org/10.1016/j.jweia.2023.105570
Received 19 December 2022; Received in revised form 14 July 2023; Accepted 13 September 2023
Available online 8 November 2023
0167-6105/© 2023 The Authors. Published by Elsevier Ltd. This is an open access article under the CC BY-NC-ND license (http://creativecommons.org/licenses/by-nc-nd/4.0/).

The complexity in studying thunderstorm downbursts is mainly twofold. Firstly, downbursts are highly transient phenomena that occur over a short time interval of 2- to 10-min duration. Their spatial extent is also limited to a few kilometers in the horizontal direction. These properties limit the available full-scale measurements of downbursts and, consequently, make it difficult to build physically realistic and reliable models as in the case of extra-tropical cyclones (Davenport, 1961). Despite the time evolution of the phenomenon being characterized in detail by deploying state-of-the-art high-sampling sensors, the spatial flow field is difficult to reconstruct due to the limited number of measuring stations. Secondly, and more relevant to this study, downburst outflows are influenced by the interaction with the background ABL winds and the translation of the parent cloud, which inherently affect the intensity and direction of surface winds. For example, Hjelmfelt (1988) and Proctor (1988) suggested that a tilted downdraft core may occur when momentum from the surrounding flow is transferred to the downdraft column. Holmes (1999) corroborates that downdrafts retain large amounts of the translational momentum of the parent cloud whose speed can be up to one third of the speed of the downdraft itself. Hjelmfelt (1988) concluded that the superposition of the low-level environment winds with the normal impinging downdraft can explain adequately the resulting outflow pattern. Fujita (1985) first reported that the travelling motion of a microburst distorts the radial symmetry of the outflow, which would otherwise be observed in the stationary case. The front-side wind (i.e., in the direction of storm motion) intensifies while the rear-side wind (i.e., against the direction of storm motion) weakens and, consequently, the outflow assumes an elliptical shape (Fig. 1). One of the evident cases of a tilted downburst is the Andrews Air Force Base microburst which was reported to have a jet axis inclined to approximately 23° from the vertical and very high horizontal wind speeds in the near-ground layer (Fujita, 1983).

Letchford and Chay (2002) used The Moving Jet Wind Tunnel at the Texas Tech University (TTU) to study the effect of the storm motion on a model cube for jet translation speeds in excess of 20% of the downdraft speed. They used a 0.51 m diameter impinging jet (IJ) (D) positioned 0.87 m (1.7D) above flat surface. The blower sat on a carriage which could be translated manually on rails at an approximately constant velocity of up to 2 m s^{-1}. A pair of switches positioned 5 m apart on the rails allowed the calculation of the jet translational speed and also provided an exact temporal and spatial reference in the velocity and pressure measurements. The length scale of the simulation was estimated to be 1:3000 based on the geometric characteristics of the facility and full-scale observations from Hjelmfelt (1988). The authors found that for translation speeds lower than 20% of the downdraft speed, no gust front was evident and the resulting outflow was very similar to a stationary wall jet. In these conditions, the smoothed velocity profile as well as the surface pressures over the cube were well approximated by a quasi-steady approach using the data from the stationary jet experiments. For higher jet translation speeds, instead, the transient characteristics significantly exceeded the quasi-steady estimates.

Fujita (1985) provided many examples of recorded microbursts where the angle of impact at the ground was between 45° and 90° to the surface due to the travelling motion of the parent storm. Mason and Wood (2005) reproduced this condition at the steady jet wind tunnel of the University of Sydney. Using a 1.82 m long horizontal settling chamber and a circular nozzle of diameter $D = 0.31$ m connected to the rectangular outlet, they produced an impinging jet on a vertical flat surface positioned 1.5D away from the outlet. The length scale was set to 1:3250 based on the nozzle diameter. They performed both steady-state and pulsed flow simulations where, for this latter, they used a punctured latex membrane to produce the vortex ring at the leading edge of the flow. Finally, the jet inclination was replicated by varying the angle of the impacting surface from the vertical position since the jet itself was unable to rotate. The authors simulated the flows over a model cube with a side length of 20 mm and found that inclining the jet generally decreases the design pressures, except for pulsed flow with the model located downwind or to the side where pressures were increased by about 5%. Later, Mason et al. (2009b) measured the outflow produced by setting the impinging jet-axis inclination to five non-normal angles from 0° to 35° and found that as the angle of the jet tilt increases, the radial extent over which high wind speeds develop also increases. Maximum wind speeds were found to be relatively independent of jet tilt, but their radial locations were observed to shift away from the jet touchdown with increasing jet tilt. The elevation of maximum wind speeds was also found to be dependent on the jet-axis angle. The authors concluded that, in terms of structural loading, tilted downbursts have the potential to cause larger loads than surface-normal events. Analogous conclusions were found by Asano et al. (2019) and Wu et al. (2021) in their experimental studies on a low-rise building and transmission line system, respectively, where they used the newly-installed moving pulsed jet simulator at the Tohoku University, in Japan, consisting of a vertical wind blower of diameter 0.6 m and height 1 m. They also found that the resulting flow field cannot be simply expressed as the vector sum of the stationary downburst wind speed distribution and the jet moving speed.

The small-scale characteristics involved in all experiments mentioned above and the use of technically restricted expedients to attempt replicating the phenomenon, leave some uncertainties on the accuracy of the results to address the actual nature of downburst winds.

In addition to the role exerted by the moving parent cloud, downbursts in nature always occur embedded in ABL winds. Indeed, under certain environmental conditions, ABL winds present pronounced velocity shears favorable for the development of thunderstorms (Burlando et al., 2017). In literature, the combination of downburst with background wind has mostly been dealt with as the vector superposition of the two wind systems (Holmes and Oliver, 2000; Chay et al., 2006; Kim

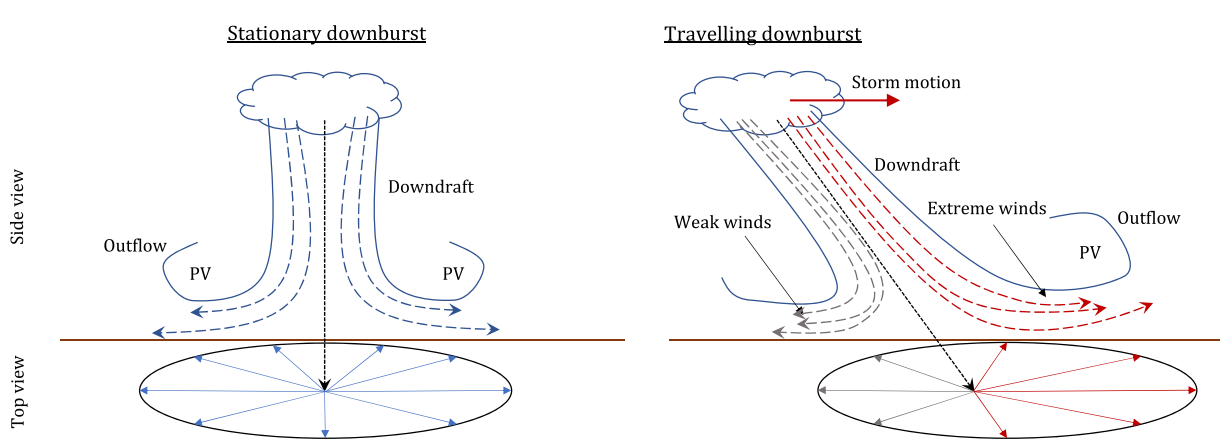

Fig. 1. Effects of the parent thunderstorm motion on the impinging downdraft and radial outflow. Adapted from Fujita (1981, 1985).

and Hangan, 2007; Abd-Elaal et al., 2014). This has been demonstrated to be physically inaccurate and only recently the non-linear interplay has been addressed experimentally (Romanic and Hangan, 2020; Canepa et al., 2022a) and analytically (Moeini and Romanic, 2022). Canepa et al. (2022a) show that the interaction with the ABL-like flow produces maximum outflow velocities at the front between the opposite-directed flow. In this region, the logarithmic-like ABL profile produces horizontal vorticity concordant to that of the downburst (DB) primary vortex (PV), which leads the outflow. This leads the ABL air to be entrained into the radially advancing PV and, consequently, the horizontal flow between the lower vortex filaments and the ground to speed up. This interplay between the two flow fields produces an intensification of the maximum wind speeds that are commonly observed at the near-ground level (Goff, 1976; Hjelmfelt, 1988; Lombardo et al., 2014) with the passage of the PV. Canepa et al. (2022a) and Romanic and Hangan (2020) further discussed challenges associated with vector superposition between the two flows by examining the spatial and temporal evolution of isolated downbursts and downbursts in the ABL wind field. Our earlier research has shown that the ABL-like flow hinders the natural expansion of the radial outflow at the interface between the two wind systems. The PV travelling velocity is thus reduced while, at the same time, the entrainment of ABL air intensifies the flow underneath. On the other hand, the vertical jet that approaches the ground is tilted by the horizontal ABL winds and thus the touchdown position is slightly shifted downwind accordingly to the ABL direction. Despite the physics behind being different, the overall outflow embedded into the ABL wind assumes an elliptical shape similar to that triggered by the parent thunderstorm translation, as speculated by Hjelmfelt (1988).

In this study, firstly we assessed the effect of moving thunderstorm on the generated outflow by studying a non-vertical IJ axis. Secondly, the simultaneous reproduction of ABL winds inside the chamber allowed to couple the contributions to reconstruct the most realistic scenario of full-scale downburst occurrence. Furthermore, the geometric scale of the experiments performed at the WindEEE Dome is by an order of magnitude or so larger than in all previous studies. According to the classical definition of Reynolds number for impinging jets, Re$= V_J D/\nu$ (where V_J is the jet velocity, D is the nozzle diameter, and $\nu = 1.48 \cdot 10^{-5}\,\mathrm{m^2\,s^{-1}}$ is the kinematic viscosity of the air), the large scale characteristics lead to Re $> 1 \times 10^6$ that allows considering the flow in "fully-turbulent" regime (Xu and Hangan, 2008) and thus to be more representative of the dynamic processes involved in full-scale downbursts.

2. Experiment setup

The WindEEE Dome is a large-scale three-dimensional wind simulator capable of producing non-stationary wind systems such as downbursts, tornadoes, gusts, sheared and veered flows and atmospheric boundary layers (Hangan et al., 2017). The facility is composed of a hexagonal chamber of 25 m in diameter by 3.8 m in height (H) and is surrounded by an outer return circuit of 40 m in diameter. One hundred fans are situated on the six peripheral walls of the testing chamber; sixty of them of diameter 0.8 m each are installed in the 60-fan wall, i.e., a matrix of 4 rows by 15 columns (Fig. 2). The 60-fan wall was used to reproduce different ABL-like flows while DB-like impinging jets are generated by means of an upper chamber which hosts six fans of larger diameter (2.5 times that of the 60-fan wall fans, 2.0 m) and is connected to the testing chamber through a bell mouth. The dynamic IJ was created by first starting the six upper fans while keeping the bell mouth louvers closed. Once the upper chamber was pressurized to the desired value (approximately 3.4 hPa larger than the pressure in the testing chamber), the louvers are suddenly opened and the air is released downward into the testing chamber (Fig. 2). The diameter (D) of the bell mouth can vary from a maximum of 4.5 m to a minimum of 1.2 m by mounting a set of different size rings. In this regard, the WindEEE Dome simulator can produce downburst-like outflows at different geometric scales, from approximately 1:100 to over 1:1000 (Junayed et al., 2019; Romanic et al., 2019), and different H/D ratios. In analogy to the experiments described by Canepa et al. (2022b, 2022a), the IJ diameter investigated in the present study was set to $D = 3.2$ m; From here, $H/D = 1.19$ and the PV can fully develop as discussed by Junayed et al. (2019).

In this study, in analogy to Mason et al. (2009b), we first addressed the effect of the moving parent thunderstorm on the generated DB field by setting the inclination of the jet axis at the outlet, namely of the bell mouth louvers, to $\theta = 30°$ with respect to the normal to the ground. It corresponds to a jet that impacts the surface at 60° and falls in the range of angles observed by Fujita (1985) during most of his full-scale observations on microbursts. The decomposition of the inclined jet velocity (V_J) into vertical downdraft velocity (V_D) and horizontal translation velocity (equivalent storm motion velocity, V_S) components evaluated through $V_D = V_J \times \cos(\theta)$ and $V_S = V_J \times \sin(\theta)$, leads to $V_S = 0.58 \times V_D$ which is in the range of values $V_S > 0.2 \times V_D$ estimated by Letchford and Chay (2002). For these values of V_S, the transient features of the phenomenon become significant and cannot be assessed through the quasi-steady theory. Fig. 2 schematically shows the formation and

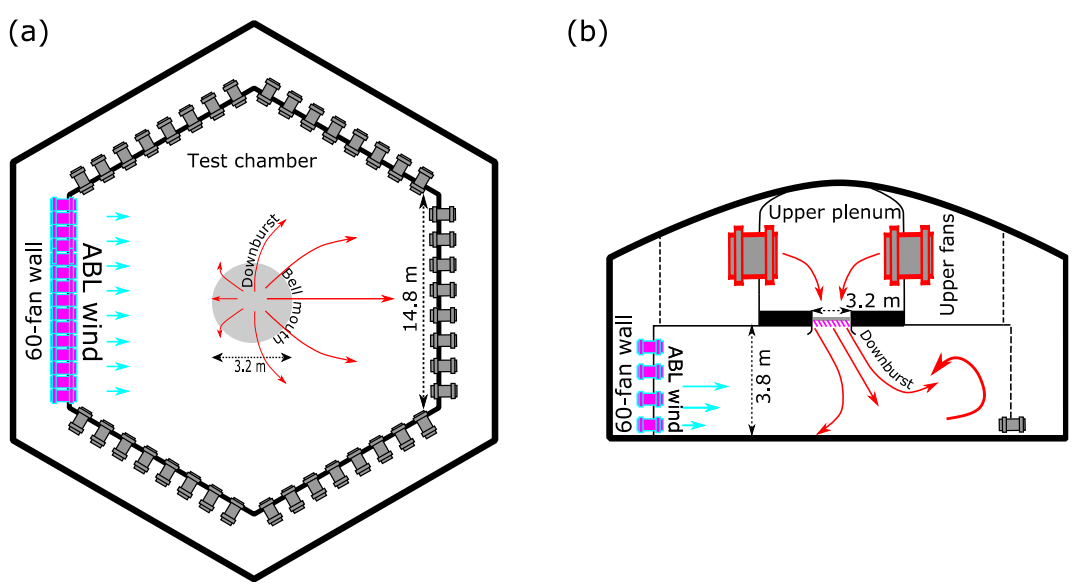

Fig. 2. Schematics of inclined downburst released into the background ABL flow in the WindEEE Dome: (a) top view and (b) side view.

scenario of inclined-jet downburst embedded in ABL-like flow.

The WindEEE Dome is also capable of simultaneously producing different ABL winds and DB outflows at various Reynolds numbers and momenta ratios of the two flows (Romanic et al., 2019). In this advanced mode, the impinging jet is released into a perpendicular ABL wind. The match of the geometric scale between downburst and ABL flows at the WindEEE Dome is addressed by Canepa et al. (2022a).

The IJ axis is inclined toward the same direction of the outgoing ABL flow. The opening of the louvres at the bell mouth of the WindEEE Dome is limited between fully closed and fully opened following the inclination shown in Fig. 2b. Hence, inclinations of the jet towards the incoming ABL wind were not possible. The DB-like impinging jet was released respectively in a calm environment, i.e., no background flow, and in an already developed ABL-like wind. Hereafter, these new cases will be named respectively inclDB and inclDBABL in order to make a clear distinction from the downburst configurations related to the vertical IJ (Canepa et al., 2022a, 2022c, 2022a). Following the same nomenclature criterion, these will be named hereafter vertDB and vertDBABL.

Analogously to the experiments described by Canepa et al. (2022c, 2022a), the intensities of ABL and IJ flows were both set to 30% of the nominal power of the respective fans. The corresponding jet velocity at the exit of the bell mouth is 12.4 m s^{-1} for inclDB and 11.8 m s^{-1} for inclDBABL. Despite the same power set at the six upper fans creating the DB-like flow, the variation between the jet velocities is due to the closed-circuit nature of the WindEEE Dome which produces a deficit in the momenta of both flows when they are generated simultaneously (Romanic et al., 2019). The inclination of the jet velocity vector to 30° produces an additional horizontal velocity V_S of 6.2 m s^{-1} and 5.9 m s^{-1}, respectively for inclDB and inclDBABL, which represents the storm translational velocity and again reflects what commonly observed in nature. The ABL-flow velocity at the outlet section (3 m downstream) of the 60-fan wall is 3.9 m s^{-1} at $z = 0.25$ m above the floor (Romanic et al., 2019). Conversely to classic boundary layer wind tunnels (BLWT), WindEEE Dome reproduces a number of different ABL-like profiles by mechanically and individually controlling the rotation-per-minute (rpm) of the 60-fan wall fans. Romanic and Hangan (2020) demonstrated that, despite the match with standard ESDU (Engineering Sciences Data Unit) ABL profiles is not achieved particularly in terms of turbulence intensity, the ABL-like profile generated with the chosen 60-fan wall configuration is consistent with the full-scale ABL wind that develops in unstable atmospheric conditions. The reader can refer to Canepa et al. (2022a) for a complete overview of the ABL vertical profiles at the measurement locations described in the following of this section. The roughness length in the proximity of the chamber geometric center was $z_0 = 3.7 \times 10^{-5}$ m. The characteristic wind speeds involved in this study are reported in Table 1.

Ten Cobra probes were deployed in each experiment and mounted on a heavy and stiff mast that prevented vibrations of the instrumentation during the tests. The mast was moved across the chamber along 10 radial (r/D) and 7 azimuthal (α) positions accordingly to Fig. 3 in order to cover a very large spatial domain of measurements, namely r/D spanning from 0.2 to 2.0 with a radial increment of 0.2 and α from 0° to 180° with an azimuthal increment of 30°. $r/D = 0.8$ is actually measured at $r/D = 0.75$ due to irregularities of the chamber bare floor in correspondence of the turntable edge, located at $r/D = 0.8$, which may distort the

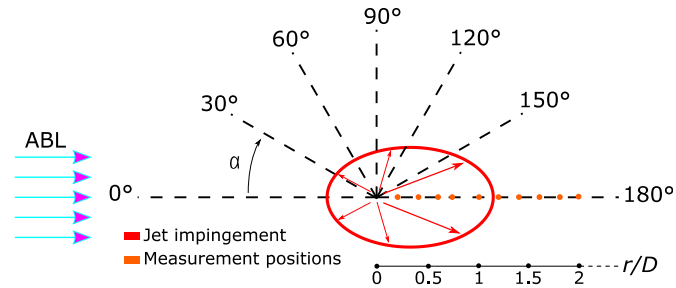

Fig. 3. Top-view schematics of inclined downburst supplemented with ABL flow.

flow measurements due to the malposition of the Cobra probe mast. Fig. 3 shows that $r/D = 0$ corresponds to the jet touchdown position when the DB is not embedded into the ABL flow (vertDB and inclDB cases), while $\alpha = 0°$ identifies the direction of the incoming ABL wind in the cases vertDBABL and inclDBABL. Due to the circular symmetry with respect to the incoming ABL direction, the results can be mirrored to the other half of the measurement circle, i.e., $\alpha = 180°–360°$. The ten probes faced the jet impingement position to measure the radial component of the wind speed and were located at heights $z = 0.04$, 0.07, 0.10, 0.125, 0.15, 0.20, 0.30, 0.40, 0.50, and 0.70 m. The horizontal and vertical distances are normalized by $D = 3.2$ m and $z_{max} = 0.1$ m, respectively, to be consistent with the analyses reported in Canepa et al. (2022c, 2022a) on vertDB, where the overall maximum horizontal velocity in the flow field was found at $z = 0.1$ m. For every α and r/D position, each experiment with the same initial conditions was repeated 10 times in order to inspect the statistical repeatability of the tests. Each experimental run is a physical realization of the phenomenon. The relatively small number of records limits the statistical estimation of the results particularly when addressing non-stationary flows. However, considering cost and time expensiveness of multiple large-scale experimental repetitions, 10 runs were considered a good compromise to provide statistical spread of the results. Therefore, 2 experiment setups × 7 azimuthal positions × 10 radial positions × 10 measuring probes × 10 repetitions resulted in 14,000 velocity records. Fig. 3 shows the measurement locations while Table 1 summarizes the overall experimental setup. Velocity measurements were recorded at a sampling frequency of $f_s = 2500$ Hz. Cobra probes (Turbulent Flow Inc.) are designed to acquire the 3 components of the velocity within a cone of ±45° in respect to the incoming flow. Null values are recorded by the instrument when the incoming flow is outside the probe's spatial cone of measurement. These values, which at most represent a few ten-thousandth of the overall samples during the downburst-related part of the signal, are disregarded in the analyses. The accuracy of velocity and yaw/pitch measurements is ±0.5 m s^{-1} and ±1°, respectively, up to approximately 30% of turbulence intensity. In order to reproduce the transient features of downburst winds, the louvres at the bell mouth were opened and then closed 4 s later; $\Delta t = 4$ s corresponds thus to the duration of the jet release into the chamber. A new automated mechanism recently installed at the bell mouth level enabled the recording of both times of opening and closing of the louvres. The mechanism relies on an analogic signal (same f_s of Cobra probes) recording the time of complete open/close position of bell mouth louvers to the same acquisition system of Cobra probes. This

Table 1
Experiment setup: Case name; Jet diameter (D); Jet velocity (V_J) at the bell mouth outlet section; Straight flow velocity (V_{ABL}) measured at $z = 0.25$ m and 3 m downstream of the 60-fan wall; Additional horizontal velocity due to jet-axis inclination (equivalent storm motion velocity) (V_S); Azimuthal locations (α); Radial locations (r/D); Cobra probe heights (z/z_{max}); Repetitions per experiment (Reps).

Case	D [m]	V_J [m s^{-1}]	V_{ABL} [m s^{-1}]	V_S [m s^{-1}]	α [°]	r/D[a] [\]	z/z_{max} [\]	Reps
inclDB	3.2	12.4	\	6.2	0:30:180	0.2:0.2:2	0.4, 0.7, 1.0, 1.25, 1.5, 2.0, 3.0, 4.0, 5.0, 7.0	10
inclDBABL	3.2	11.8	3.9	5.9	0:30:180	0.2:0.2:2	0.4, 0.7, 1.0, 1.25, 1.5, 2.0, 3.0, 4.0, 5.0, 7.0	10

[a] $r/D = 0.8$ is moved to $r/D = 0.75$ due to irregularities of chamber floor.

allowed the alignment of all repetitions of the same experiment and, furthermore, the overall synchronization of all signals across the measurement positions in the chamber to thoroughly inspect the spatial and temporal evolution of the downburst system.

To obtain an actual correspondence with the time duration and evolution of full-scale downburst records, a normalized time $\tau = t \cdot f_v$ was introduced based on the frequency of vortex shedding from the bell mouth, f_v. The vortex shedding frequency was defined based on the Strouhal number definition ($St = f_v \cdot D/V_J$) for round impinging jets, $St = 1.2(x/D)^{-1}$ (Popiel and Trass, 1991). x defines the distance from the bell mouth inlet section to the testing chamber floor, $x = 5.35$ m. From this simplified expression we obtain $St = 0.72$, which is slightly greater with respect to the range of values 0.35–0.65 reported in previous experimental studies at lower Re ($O(10^4–10^5)$) and scales (Hadžiabdić and Hanjalić, 2008) and resumed by Canepa et al. (2022c). The St definition above returns a vortex shedding frequency $f_v = 2.65$ and 2.79 Hz for the two V_J involved in the cases of inclDBABL and inclDB, respectively. This provides that, due to the dynamic instabilities between jet and surrounding calm environment, an eddy structure (vortex) forms at the bell mouth level each $t_v = 1/f_v \cong 0.37$ s. It follows that approximately 10 vortices shed during the experimental downburst release $\Delta t = 4$ s, which corresponds to $\tau \cong 10$. To obtain a full-scale equivalency with respect to this analysis, as first approximation we may consider a 10-min downburst record, meaning that the presence of a velocity ramp-up and transient peak is clearly detectable in 10 min. Burlando et al. (2018) concluded that the events classified as 10-min records were the majority of the overall 277 downburst signals analyzed. To adopt the same formulation of Popiel and Trass (1991) introduced above, a release (inlet section) height and diameter of an ideal full-scale downdraft should be defined. Considering a thunderstorm cloud (cumulonimbus) vertical development from few km above the ground level, say 2 km, up to approximately the top of the troposphere, say 10 km, the downdraft release section may be assumed at the center of the cloud vertical extension, i.e., $x_{FS} = 6$ km. The downdraft diameter D_{FS} may be assumed in the order of 1.5 km (Hjelmfelt, 1988), while its downward vertical velocity $V_{J,FS}$ at the inlet section in the order of 20 m s^{-1}, also relying on the approximate ratio of 1.5 between the maximum horizontal velocity at the near-ground level and the jet vertical velocity (Canepa et al., 2022c). These first-approximation parameters lead to $St \cong 0.3$, $f_v \cong 0.04$ Hz, and $t_v \cong 250$ s. It follows that approximately 2.5 vortices are shed in a 10-min downburst occurrence. Therefore, the 4-s experimental records here analyzed widely cover the development of a downburst event in nature and allow a thorough investigation of the signal also in the frequency domain.

Following the definition above, τ depends on the jet velocity V_J of the specific experimental configuration under investigation. For comparison purposes between the experimental cases of inclDB and inclDBABL (and with vertDB and vertDBABL), an average jet velocity $\overline{V}_J = 12.1$ m s^{-1} and consequent shedding frequency $\overline{f}_v = 2.72$ Hz was defined to display a shared τ in the related graphic outcomes.

3. Results

If not otherwise specified, the wind speed values shown in the following refer to the slowly-varying mean component $\overline{V}$ computed by filtering the original wind velocity time series with a mobile averaging window of $T = 0.1$ s (Junayed et al., 2019). This choice of T comes from a compromise: if T is too large, the residual fluctuation $V'(t) = V(t) - \overline{V}(t)$ retains part of the large scale wind structure; if T is too small, the time-varying mean velocity $\overline{V}(t)$ retains turbulence fluctuations at the small scale (Solari et al., 2015). The reader can refer to Solari et al. (2015) for a complete overview of the downburst velocity decomposition process. The results will spatially refer to the regions here named rear and front, corresponding to measurements between $\alpha = 0°–90°$, and $\alpha = 90°–180°$, respectively.

3.1. Space and time reconstruction of DB flow fields

All wind speed records were synchronized based on the time of complete opening of the bell mouth louvres. Fig. 4 shows wind speed time series at $r/D = 1.0$ and selected α and z locations in the flow field. The two x-axes allow a clear comparison between experimental and normalized time evolution of the signals, and to draw conclusions with respect to the full-scale scenario based on the considerations reported in Section 2. At $\alpha = 0°$ the differences between inclDB and inclDBABL are pronounced and due to the strong mixing between the two counter-directed flows. Elsewhere, the velocity signatures between the two cases are similar and almost overlapping each other, with some detachment at the front-wind side due to the jet axis inclination and inclusion of the ABL-like wind. The following of this section will deeply address the mutual interplay between DB and ABL flows. Particularly at $\alpha = 90°$, that is the measurement location less affected by the asymmetries introduced in the downburst system by the jet-axis inclination and superposition with ABL-like flow, the three segments of the downburst signal introduced by Canepa et al. (2022b) are clearly detected: (1) the PV segment, including the wind speed ramp-up and peak due to the passage of the PV over the measuring instrument; (2) the plateau segment, where the flow is governed by smaller trailing vortices following PV and the mean wind speed is quite stationary in time; (3) the dissipation segment, where the downburst phenomenon dissipates or travels away from the instrument. After the dissipation segment, the wind speed of inclDBABL is not observed to promptly return to the original values before the onset of the DB flow. This is evident at the front side of the measurement domain where Cobra probes are oriented against the incoming direction of the ABL flow as well. After the termination of the IJ, in fact, the flow inside the chamber undergoes a transition phase before returning to ABL-regime conditions (beyond the time domain represented in Fig. 4). The non-zero values of inclDB before and after the opening and closing of the bell mouth, respectively, may be due to some leakage at the bell mouth level while the upper IJ fans are running.

In Fig. 5i, the overall radial symmetry is lost and the outflows assume an elliptical shape as reported by Fujita (1985), among others. Indeed, the downdraft inclination at the ground intensifies the flow in the front-wind region and weakens it in the rear-wind part, according to our nomenclature.

The absolute maxima of the slowly-varying mean wind speed occur at the locations $\alpha = 150°$, $r/D = 1.4$, $z/z_{max} = 0.4$ and $\alpha = 90°$, $r/D = 1.0$, $z/z_{max} = 0.7$ for the cases of inclDB and inclDBABL, respectively, compared to $r/D = 1.0$, $z/z_{max} = 1.0$ for vertDB (radial symmetry) and $\alpha = 30°$, $r/D = 0.75$, $z/z_{max} = 0.7$ for vertDBABL. At these locations, the absolute maximum and the standard deviation of the maxima across the 10 experimental runs assume the following values: $\overline{V}_{max} = 19.78$ m s^{-1} and $\sigma_{\overline{V},max} = 0.65$ m s^{-1} (inclDB); $\overline{V}_{max} = 18.62$ m s^{-1} and $\sigma_{\overline{V},max} = 0.51$ m s^{-1} (inclDBABL); $\overline{V}_{max} = 13.88$ m s^{-1}and $\sigma_{\overline{V},max} = 0.34$ m s^{-1} (vertDB); $\overline{V}_{max} = 22.86$ m s^{-1}and $\sigma_{\overline{V},max} = 0.34$ m s^{-1} (vertDBABL). Note that in the case of vertDB lower IJ velocities were used (Canepa et al., 2022b). Also supported by parallel CFD simulations of the experimental scenario at the WindEEE Dome (Žužul et al., 2022), the weaker outflow in the rear side of inclDB, caused by the downdraft tilting at the touchdown towards $\alpha = 180°$ (front-wind region), may lead to a less symmetric and more complex PV structure which, consequently, may not entrain the ABL air (inclDBABL) as pronouncedly as in vertDBABL (Canepa et al., 2022a) (Fig. 5ii). For this reason, the flow speed-up effect in the rear region somewhat vanishes. At the position of overall maximum velocity in the flow field for vertDBABL, the 10-repetition ensemble of maximum velocities is $\overline{V}_{max} = 17.36$ and 22.34 m s^{-1}, respectively for inclDBABL and vertDBABL. This implies a velocity reduction of about 22% in inclDBABL with respect to vertDBABL due to the different interaction between the two flows. The ABL flow rather tilts the inclined downdraft (inclDBABL) in the front region to a larger angle with respect to that

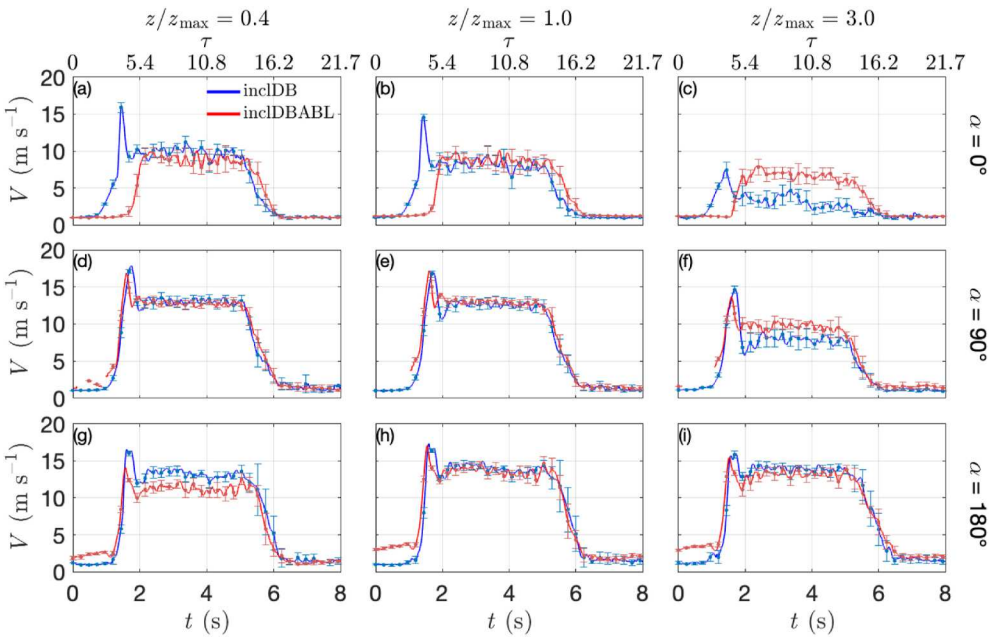

Fig. 4. Velocity time histories at $r/D = 1.0$ and different α and z locations for inclDB (blue lines) and inclDBABL (red lines). Thick lines and error bars represent the ensemble mean and standard deviation of the 10 experimental runs, respectively.

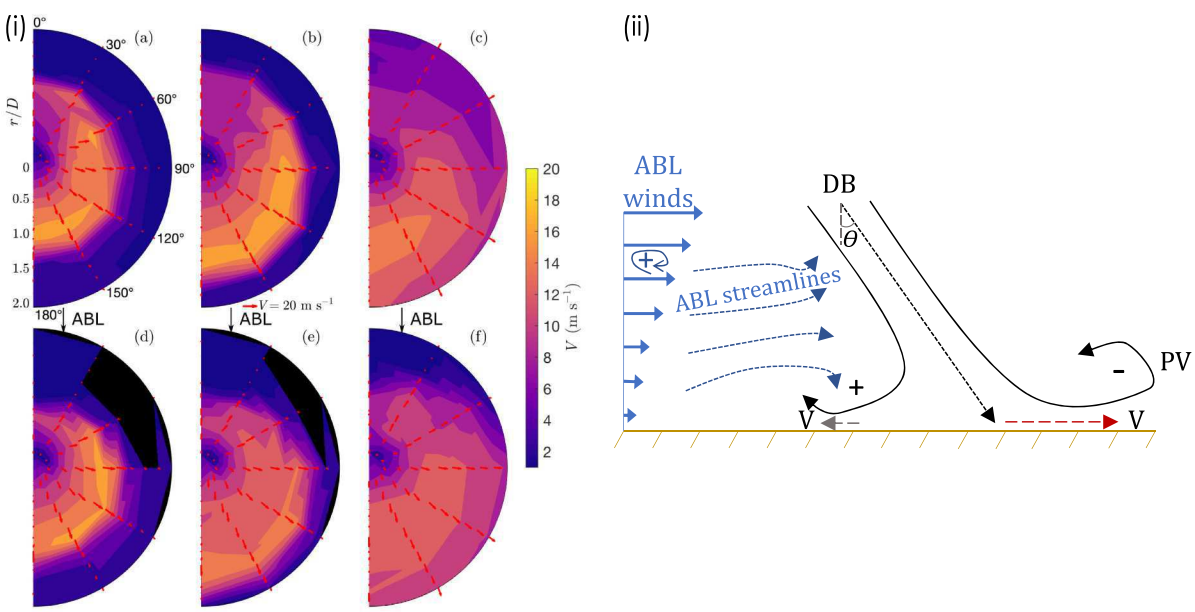

Fig. 5. (i) Downburst outflow field at $z/z_{max} = 1.0$ (horizontal plane $r - \alpha$) and $t = 1.60$ s ($\tau = 4.4$) (a,d); $t = 1.83$ s ($\tau = 5.0$) (b,e) and $t = 3.00$ s ($\tau = 8.2$) (c,f) for inclDB (a–c) and inclDBABL (d–f) cases. Black spots identify regions where velocity is below 1 m s^{-1} (not considered due to accuracy of probes). Red vectors are Cobra probe measurements while the overall flow fields are obtained from their interpolation. (ii) Schematics of the DB-ABL interaction (vertical plane as seen from $\alpha = 270°$). $\pm$ indicate the sign of vorticity.

provided by the experimental setup, $\theta > 30°$. The touchdown position and, thus, the DB outflow region is shifted towards $\alpha = 180°$ accordingly. In the rear-wind side, the flow is spatially hindered by the counter-directed ABL flow which limits the outflow and PV expansion. While intensifying, the PV is observed to remain stagnant at the same approximate radial position throughout the time evolution of the phenomenon. This is clear by observing the location of the high wind speed area (tracking the passage of PV) in Fig. 5i(e) and Fig. 5i(f) (time gap $\Delta t = 1.17$ s, $\Delta\tau = 3.1$ between the two scenarios) and by inspecting flow visualization tests conducted at the laboratory (not shown here). It is inferred that the interaction with DB in the rear region forces the ABL to deviate outwards and exit the chamber through the lower peripheral fans. In this region, the lower velocities of inclDBABL with respect to inclDB also relate to the deficit in the momentum of the impinging jet when produced simultaneously with the ABL flow (Romanic et al., 2019).

Fig. 6 shows the envelope of maximum wind speeds (related to the passage of the PV) as recorded at each (α, r/D) location and at heights $z/z_{max} = 0.4$, 1.0, 2.0, and 5.0 (panels A–D) of all tested cases. The speed-up effect due to the entrainment of ABL flow (panels b,d) into the

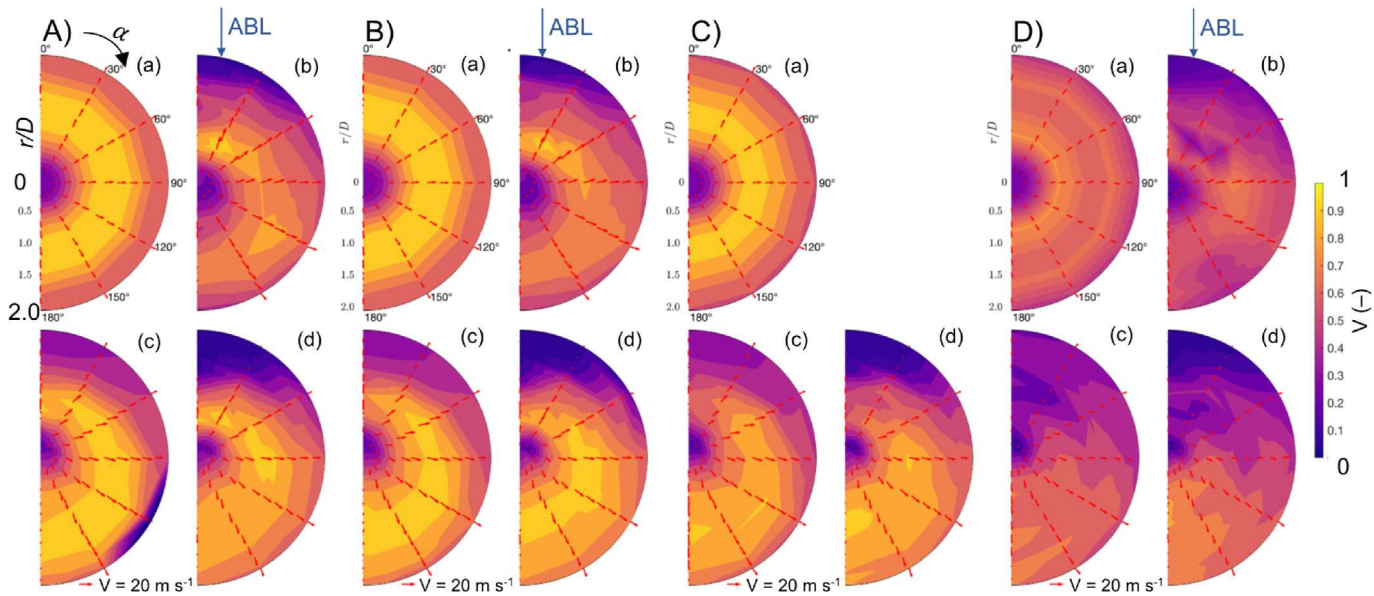

Fig. 6. Downburst outflow field (horizontal plane $r-\alpha$) of maximum velocity envelops at $z/z_{max} = 0.4$, 1.0, 2.0, and 5.0 (panels A–D) for vertDB (a), vertDBABL (b), inclDB (c) and inclDBABL (d) cases. Red vectors are the maximum wind speeds as measured by Cobra probes while the overall flow fields are obtained from their interpolation. The case vertDBABL was not measured at $z/z_{max} = 2.0$.

counter-directed PV in the rear region (Fig. 5ii, see also Canepa et al., 2022a) is highlighted at the height $z/z_{max} = 0.4$ (panel A). Accordingly, the maximum horizontal velocities are experienced at $\alpha = 30°$ and $r/D =$ 0.75–1.0. From $z/z_{max} = 1.0$ (panel B) the inclDBABL case loses the benefit of ABL entrainment and the region of highest wind speeds moves to the front side due to the jet-axis inclination and concordant direction of DB and ABL in this area. Nevertheless, the case of vertDBABL still shows the highest velocities in the rear part. At $z/z_{max} = 2.0$ and 5.0 (panels C,D), inclDB and inclDBABL (panels c,d) show very similar distributions of maximum wind speed values, meaning that the IJ-axis inclination becomes the dominant contribution to the maxima of the velocity. The intensification of the front-side wind speeds is clear at any height for the case inclDB.

The same concept holds for Fig. 7, which shows the envelope of time-averaged horizontal wind speed over the plateau segment. The average was computed over a time interval of 1.5 s (3750 samples) starting 0.2 s (500 samples) after the end of the PV segment. The intensification of the rear-wind side due to the ABL entrainment is noticed only for vertDBABL and at the lowest height (panel A(b)), whereas it is lost at the higher elevations where vertDBABL assumes a quasi-symmetric behavior similar to vertDB. However, one should also bear in mind that by performing a time average across the plateau segment and ensemble mean across repetitions, unphased trailing vortex structures and related peaks in the velocity signals are filtered out from the final ensemble. In analogy to the PV segment, the wind speed decreases along the height due to the outflow dynamics upon impingement and funneling of the flow beneath the vortical structures (see Fig. 5ii and Canepa et al., 2022c).

Fig. 8 shows the spatial pattern of inclDB and inclDBABL outflows in the vertical plane $r-z$ at azimuthal positions $\alpha = 0°$, 90°, and 180° at a given moment in time ($t = 1.72$ s, $\tau = 4.7$) between the occurrences of the wind speed maxima of the two cases. The inclusion of ABL wind (panels d–f) does not change considerably the velocity magnitudes but

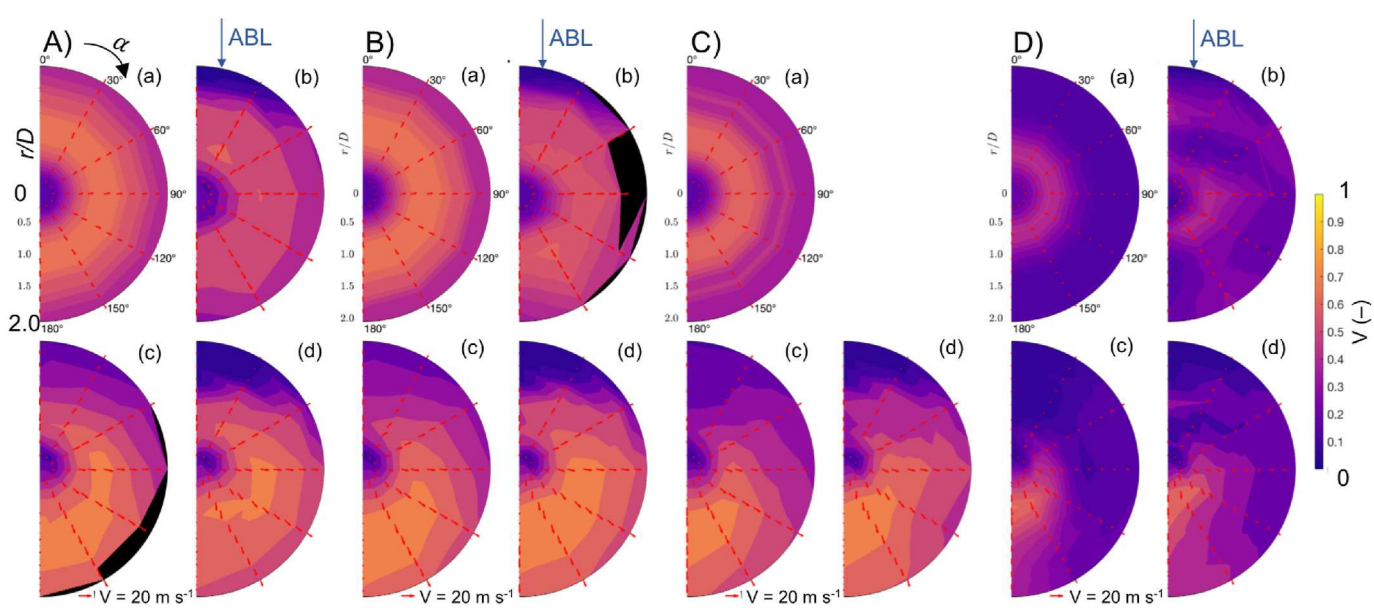

Fig. 7. Same as Fig. 6 but for envelops of plateau temporal-mean horizontal wind speeds.

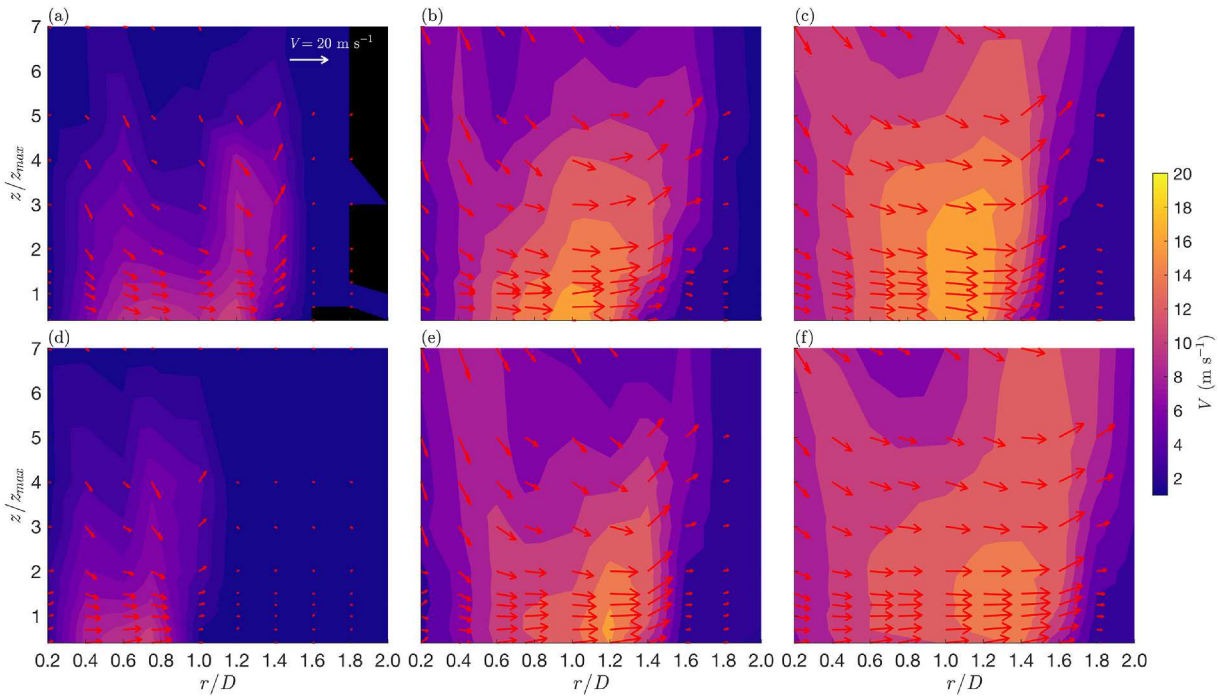

Fig. 8. Downburst outflow field (vertical plane $r-z$) at $t = 1.72$ s ($\tau = 4.7$) and $\alpha = 0°$ (a,d), 90° (b,e), and 180° (c,f). Upper (a–c) and bottom (d–f) graphs show the case inclDB and inclDBABL, respectively. Black spots identify regions where velocity is below 1 m s^{-1} (not considered due to accuracy of probes). Red vectors are Cobra probe measurements while the overall flow fields are obtained from their interpolation.

shifts the position of the outflow according to the mutual interaction between the different flow components. At $\alpha = 0°$ (panels a,d) the interface between DB-ABL curbs the PV radial expansion which in Fig. 8d is recorded approximately $\Delta r/D = 0.5$, in terms of radial interval, behind with respect to inclDB (Fig. 8a). The situation is reversed in the front-wind side where PV is radially ahead in inclDBABL compared to inclDB. Here, the slight velocity reduction in inclDBABL with respect to inclDB may be due to the opposite flow circulation of ABL and PV at the front-wind side (see Fig. 5ii).

3.2. Non-linearity in superposition of effects

The non-linearity of the superposition of stationary downburst (V_{SDB}), ABL flow (V_{ABL}) and storm translation (V_S) is clearly depicted in Fig. 9 for the several cases tested during the experimental campaign. V_{SDB} and V_{ABL} at the different measurement locations are acquired within the same experimental campaign and can be found in the literature (Canepa et al., 2022a, 2022b, 2022a). V_S is defined in Section 2 as a vector directed towards $\alpha = 180°$, constant along the height, and equal to 6.2 m s^{-1} and 5.9 m s^{-1}, respectively for inclDB and inclDBABL. As expected, actual measurements are higher than corresponding values

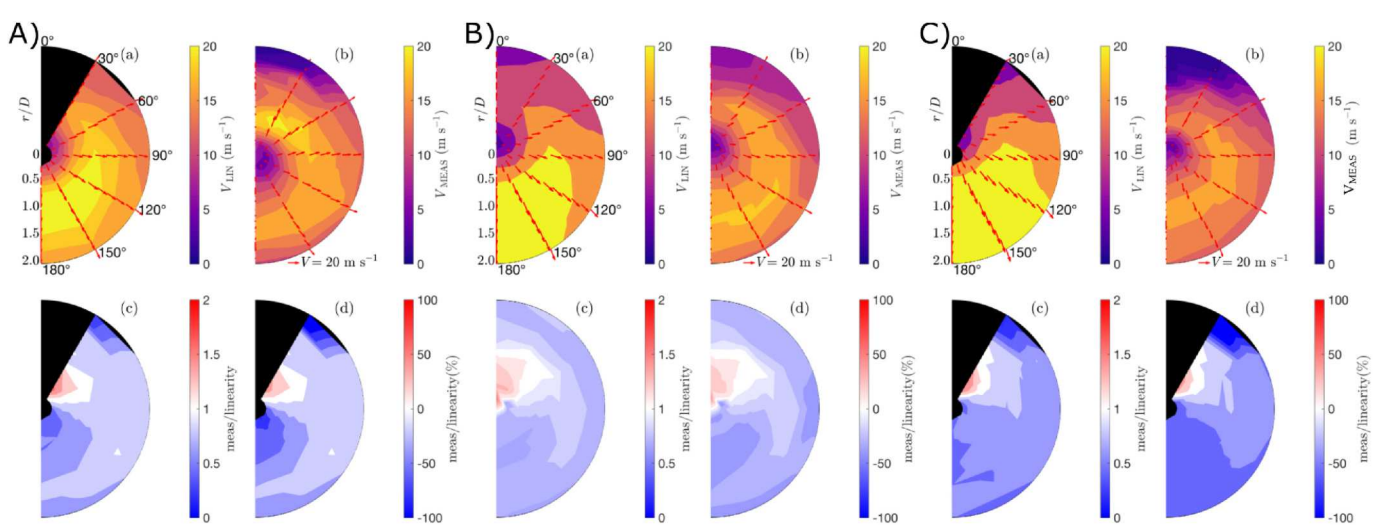

Fig. 9. Measurements (panels b) vs. linear superposition (panels a) of velocity flow components at the time of peak velocity at $z/z_{max} = 1.0$, for vertDBABL (A), inclDB (B) and inclDBABL (C). Ratio between measurements and linear superposition (panels c) and their percentage difference (panels d). Black spots identify either regions where velocity is below 1 m s^{-1} (not considered due to accuracy of probes) or where linear superposition cannot be performed due to missing measurements of ABL flow at the specific location. Red vectors are actual Cobra probe measurements (panels b) or vectorial sum of component vectors (panels a), while the overall flow fields are obtained from their interpolation.

resulting from vector combination at the rear-wind side. This is particularly due to the non-linear effect of ABL entrainment in the PV structure and consequent flow enhancement (Fig. 9A,C). However, the same concept partly holds also for inclDB case (Fig. 9B) where no ABL is present. The vector superposition considers V_{SDB} which was measured only at $\alpha = 90°$, due to the circular symmetry of stationary vertical DB, and with a different jet velocity compared to the present experiments. The latter of these shortcomings is taken into account by a correction factor that considers the almost identical ratio between maximum horizontal wind speed at the specific location of measurement and jet velocity for the different jet intensities that were used in the stationary case. However, the non-symmetrical opening of louvres at the bell mouth (clockwise if seen by an observer ideally at $\alpha = 270°$) may produce a horizontal momentum toward $\alpha = 0°$ that increases the flow speed in the rear-wind region, even in absence of ABL wind. The same discrepancy between real and theoretical values is not observed at the top measurement heights (not shown here), which are at the lower boundary of the PV structure (Junayed et al., 2019). Here, the ABL entrainment does not occur as regularly as at the near-ground region and, also, the momentum due to the opening of louvres is less pronounced.

The difference between measured and linearly superimposed flows is large at $\alpha = 0°$–$30°$ and up to $r/D = 1.0$, whereas outside this area the values are similar and the ratio between the two quantities is close to 1. Around the region of $\alpha = 90°$, where the asymmetry due to the ABL flow and jet axis inclination (both directed along the line $\alpha = 0°$–$180°$) is weak, the two values match reasonably well. Larger differences are again noted in the front-wind region but now reversely, with linear reconstruction presenting higher values compared to actual measurements. The nonlinear interaction between DB and ABL, as well as the asymmetric opening of the bell mouth louvres described above, make the actual flow weaken at the front-wind side. However, the asymmetric behavior of ABL seems to play a more relevant role to this end as the inclDB case (Fig. 9B) has still ratio values close to 1.

3.3. Characteristics of outflow vertical profiles

The analysis of full-scale downburst events has clearly shown that at the moment of maximum intensity, associated with the passage of the gust front, the wind speed vertical profile assumes a transient nose-like

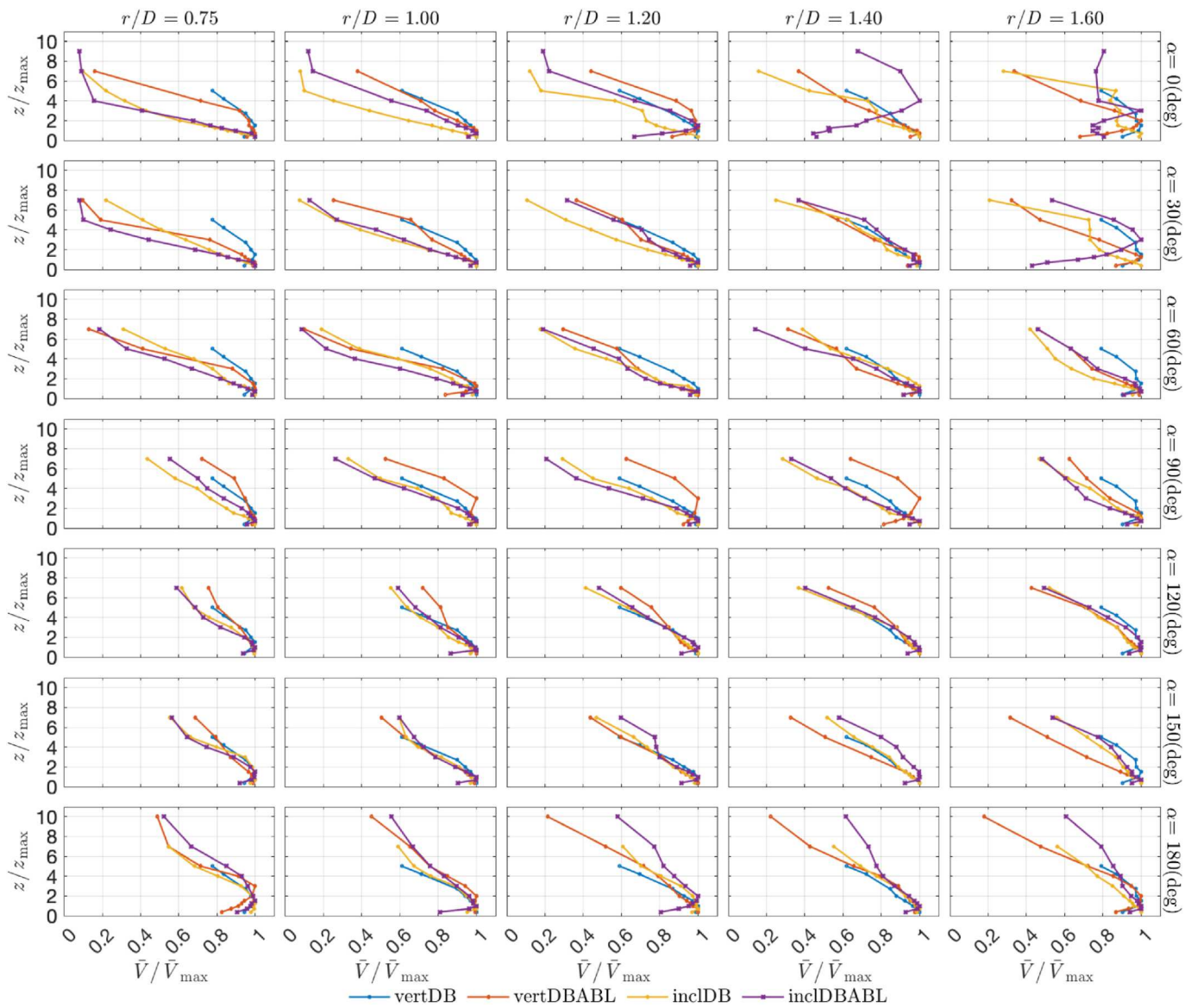

Fig. 10. Vertical profiles of slowly-varying mean wind speed $\overline{V}$, normalized by its case-related maximum value $\overline{V}_{max}$, at the time of the peak for $r/D = 0.75$–1.60 and all α locations.

shape with maximum horizontal wind speeds in the range 50–120 m above the ground level (AGL) (Goff, 1976; Canepa et al., 2020).

The vertical profiles of the slowly-varying mean wind speed, $\overline{V}$, at the time of its maximum at the specific azimuth and radial location of measurement (Fig. 10) provide an indication of the wind loading and effects on structures. The first and important feature to note is that the nose-like shape appears clearly in all cases and at all measurement locations. At the interface between DB and ABL, the outflow vertical profiles show the height of the nose, i.e., height of maximum slowly-varying mean wind speed $z(\overline{V}_{\max})$, at higher elevations for inclDBABL and partly vertDBABL compared to the other cases. At $\alpha = 90°$, this latter case shows higher $z(\overline{V}_{\max})$ and a vertical profile that differentiates largely from the other cases. In general, however, the profiles along height show similar pattern, with the exception of $\alpha = 0°$. Here, the large asymmetry caused by the embedment of ABL into the DB outflow and by the inclination of IJ axis makes the profiles deviate considerably. At the front-wind side, the different cases show similar profiles with some deviation at $\alpha = 180°$ particularly due to the IJ-axis inclination.

Fig. 11 shows the time variation of $z(\overline{V}_{\max})$. This analysis considers only the radial flow region where the PV passage is reported in all signal repetitions, i.e., $r/D = 0.6$–1.4. This excludes the locations either inside or far away from the downdraft stage which are characterized by a quite high variability among experimental repetitions. Upon aligning all signals, ensemble average of $z(\overline{V}_{\max})$ was performed across experimental repetitions and all radial and azimuth locations of measurement (Fig. 11a) as well as individually per azimuth location (Fig. 11b–d). The diagrams show results up to $\tau = 10$ due to the different length of plateau segments at the different measurement locations.

An analogous trend is observed among DB cases in Fig. 11a, where $z(\overline{V}_{\max})$ is observed at high levels $z/z_{\max} > 2.0$ at the beginning of the velocity signals. In vertDBABL and inclDBABL this behavior is produced by the logarithmic-like vertical profile of the ABL flow which is started prior to the release of the IJ. This aspect is very clear at the locations where the Cobra probes are oriented against the ABL flow and can properly measure its vertical profile (Fig. 11d). Analogously to what was reported by Canepa et al. (2022c), the high elevations of $\overline{V}_{\max}$ in vertDB and inclDB might be due to viscous effects that arise in the near-surface region producing flow slow-down at the lower levels and consequent acceleration above. This behavior is enhanced at the front-wind side following the flow intensification due to the jet-axis inclination (Fig. 11d). Moving forward in time, $z(\overline{V}_{\max})$ is observed to drop drastically concurrently with the passage of PV. At this point, the flow streamlines are squeezed near the surface producing an increase in wind speed and a decrease in the height of maximum. This evolution may have implications on the loading of structures and certainly deserves future research. In the two cases of DB embedded in ABL flow (vertDBABL and inclDBABL) $z(\overline{V}_{\max})$ is here recorded respectively at $z/z_{\max} = 1.12$ and 1.22, which is rather higher with respect to vertDB and inclDB, both slightly lower than $z/z_{\max} = 1.0$. The PV indeed raises over the ground by entraining ABL air and increasing its size and vorticity. From here $z(\overline{V}_{\max})$ settles to an approximately constant value which lasts throughout the plateau phase. At $\alpha = 90°$ (Fig. 11c) which is the location least influenced by the flow asymmetries, the height of maximum velocity shows a very similar behavior across all cases throughout the duration of the event. At the plateau segment of the velocity in the front-wind region (Fig. 11d), the upward momentum produced by the IJ

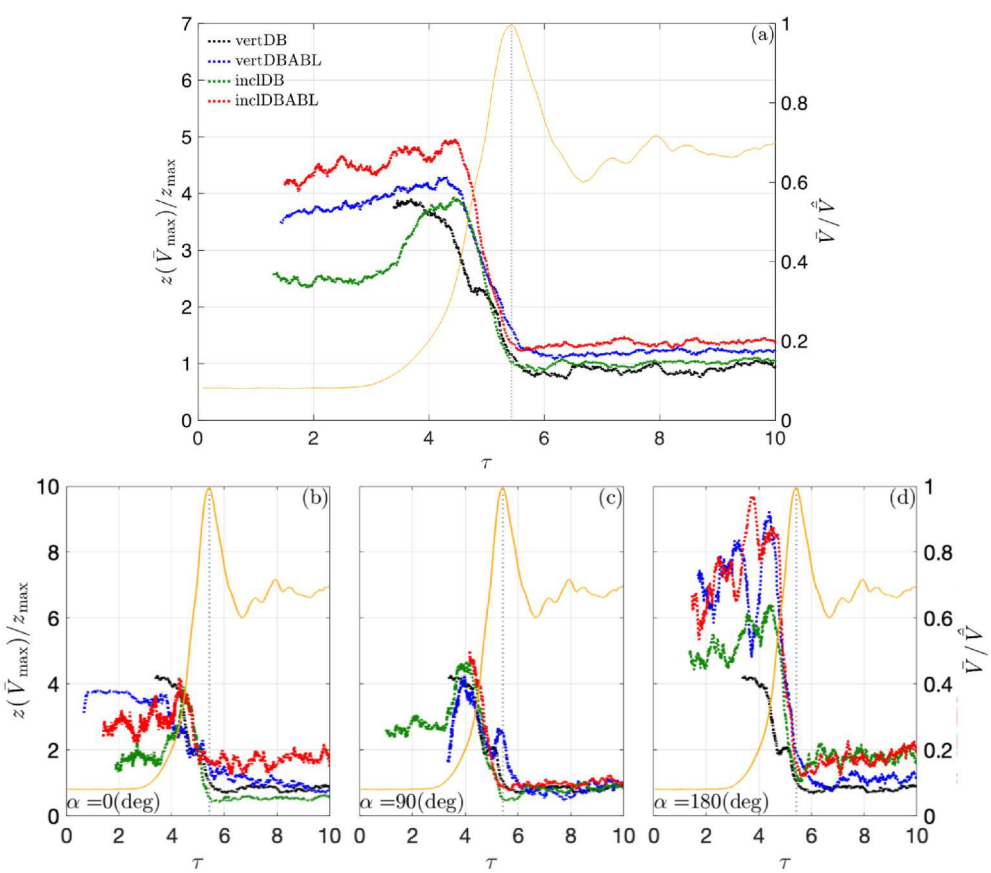

Fig. 11. (a) Time histories of $z(\overline{V}_{\max})$, evaluated as ensemble mean across all repetitions, azimuth locations and radial locations $r/D = 0.6$–1.4, for vertDB, vertDBABL, inclDB, and inclDBABL. Orange line shows the ensemble average of the 20 slowly-varying mean velocity repetitions at ($r/D = 1.0$, $z/z_{\max} = 1.0$) for vertDB; the slowly-varying mean wind speed $\overline{V}$ is normalized by its absolute maximum value $\widehat{\overline{V}}$ (right-hand secondary y-axis). The vertical gray dotted line shows $\tau(\widehat{\overline{V}})$. (b–d) same as (a) but applied separately on the azimuthal locations $\alpha = 0°$ (b), 90° (c) and 180° (d).

inclination on the overall flow produces an increase of $z(\overline{V}_{\max})$, which is not observed elsewhere.

3.4. Turbulence characteristics

Analyses of large sets of full-scale downburst events (Solari et al., 2015; Zhang et al., 2018, 2019; Canepa et al., 2020), as well as experimentally produced downburst outflows (Romanic et al., 2020; Canepa et al., 2022a, 2022c), prove that the usual hypothesis of constant turbulence intensity in time, $I_V = \bar{I}_V$, adopted in the literature does not reflect properly the actual dynamics of the phenomenon. Here $\bar{I}_V$ is the temporal mean of the slowly-varying turbulence intensity $I_V(t) = \sigma_V(t)/\overline{V}(t)$, where $\sigma_V(t)$ is the standard deviation of the residual fluctuation $V'(t) = V(t) - \overline{V}(t)$. These studies considered the parameter $\mu(t) = I_V(t)/\bar{I}_V$ and found a local maximum and minimum respectively before and after the occurrence of the maximum horizontal velocity, associated to the passage of the PV. Compared to the full-scale environment, this aspect is highlighted in experimental conditions due to the significantly lower Reynolds numbers Re involved at the WindEEE Dome. Furthermore, Canepa et al. (2022a) shows that the embedment of DB wind into the already developed ABL contributes to adding turbulence to the overall flow field. The analysis of inclDB and inclDBABL (Fig. 12) confirms these characteristics. The maxima of $I_V(\tau)$ are observed at $r/D = 1.4$–1.8 and lowest measurement heights. As expressed by Canepa et al. (2022c, 2022a), this might relate to the onset of a secondary vortex (SV) at these radial locations and to its interaction with the PV. This trend is particularly observed for $\alpha \geq 90°$. The counter directed ABL wind in the rear-wind region may break the formation of the SV at the leading front of the DB outflow (Fig. 5ii). The fluctuations of μ are pronounced in the rear-wind region, affected by high mixing between oppositely directed DB and ABL, whereas they are reduced and quite symmetric around the mean value ($\overline{\mu} \cong 1$) in the front-wind area. The shift of the maxima of $\mu(\tau)$ between lower and higher heights may relate to the vertical growth of the SV – and thus of the boundary (or inner) layer below the PV – along the radial dimension (Canepa et al., 2022c).

Fig. 13 shows the vertical profiles of I_V at the time of maximum wind speed (Fig. 10). In the rear-wind region, the dissimilarity among profiles is quite clear. Particularly, vertDB clearly shows the lowest values of I_V. This implies that the inclusion of asymmetries into the system (ABL flow and jet-axis inclination) contributes to adding turbulence to the DB environment. In the front-wind side, where the flow mixing between components is less pronounced, I_V decreases and profiles have similar values among the cases. Similarly to full-scale recordings of downburst vertical profiles (Canepa et al., 2020), I_V assumes an increasing monotonic trend along the height. This is partly expected due to the modulation of the slowly-varying mean wind speed that is maximum in the close proximity of the ground and decreases above (Fig. 10). However, particularly in the front-wind region and for cases with ABL, high values are also observed at the ground and vertical profiles assume a C-like shape.

Turbulence intensity values appear in the range of those found by Canepa et al. (2022c, 2022a) with increasing magnitudes at the interface between DB-ABL, where I_V shows values sometimes greater than 30%. In the front-wind region, I_V decreases and oscillates around 10%. Furthermore, these values are in good agreement with those found in nature along the elevation (Canepa et al., 2020).

Also, in agreement with literature on full scale downbursts, the reduced turbulent fluctuation component $\widetilde{V}'(t) = V'(t)/\sigma_V(t)$ can be treated to a very good extent as a stationary random process with zero mean and unit standard deviation. Furthermore, this study corroborates that the pattern of the power spectral density (PSD) of $\widetilde{V}'$ (not shown here) follows the law $n^{-5/3}$ (n is the frequency) at the high frequency end, in agreement with the analyses on full scale synoptic-scale ABL winds as well as real downburst occurrences (Holmes et al., 2008; Solari et al., 2015; Burlando et al., 2017).

4. Conclusions and prospects

This paper fits into the framework of the large experimental campaign on downburst winds performed at the WindEEE Dome, at Western University in Canada, in 2019. Specifically, it draws the conclusions and main findings from analyzing the dynamic behavior of downburst winds, as reproduced in a large-scale laboratory environment. The main focus of the campaign has been on assessing the role of the different physical contributors to the overall phenomenon, first studied individually and later in a combined manner. In full-scale records, the role of the individual flow components that form the final

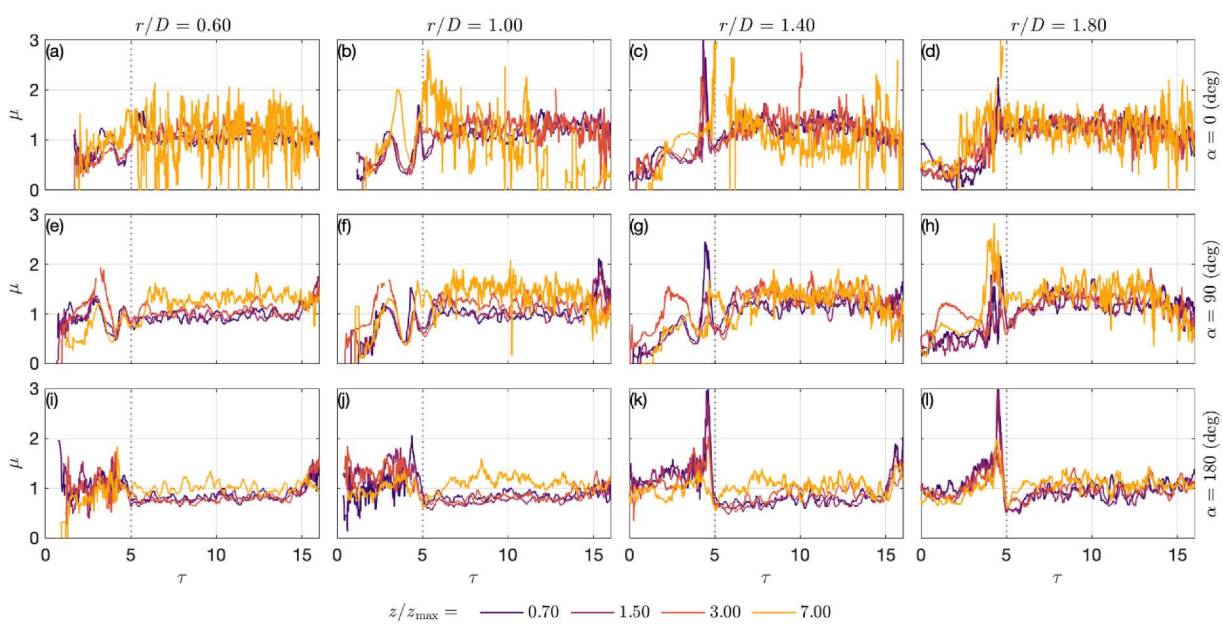

Fig. 12. Ensemble averages of 10 timeseries (experiment repetitions) of μ at $\alpha = 0°$, 90° and 180°, $r/D = 0.6$, 1.0, 1.4, and 1.8, and $z/z_{\max} = 0.7$, 1.5, 3.0, and 7.0, for inclDBABL. Vertical gray dotted lines show $\tau(\overline{V}_{\max})$.

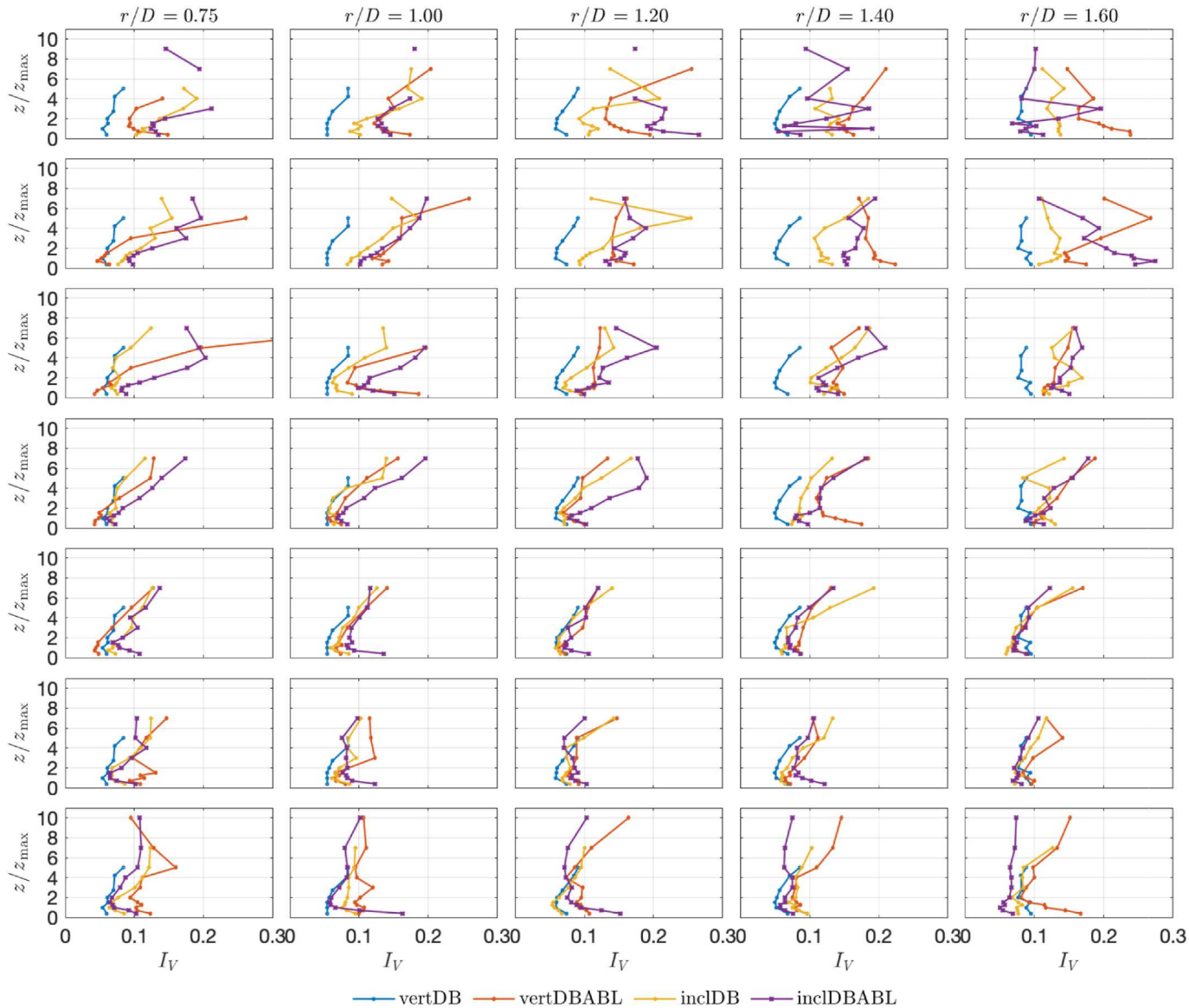

Fig. 13. Vertical profiles of slowly-varying turbulence intensity I_V at the time of peak wind speed for $r/D = 0.75$–1.60 and all α locations.

downburst wind as recorded by instruments is usually unknown. Furthermore, the very limited spatiotemporal extension of the phenomenon in nature does not allow to have a thorough view of its behavior and evolution during the occurrence of the event. However, a clear understanding of the physics and dynamics of downburst winds is crucial in view of analyzing the wind-structure interaction. It follows that only experimental and numerical models can fill this gap. The horizontal outflow that forms upon the downdraft impingement on the ground is the combination of mainly three factors: the downdraft itself, the background low-level horizontal ABL-type wind, and the storm motion or parent cloud translation. WindEEE Dome is capable to reproduce non-stationary extreme winds under a superposition of conditions at scales as large as 1:100. WindEEE can reproduce the three above-mentioned flow contributes individually: the downdraft is reproduced through an impinging jet (IJ) that blows through a bell mouth installed on the ceiling of the testing chamber; the background ABL flow is supplied by means of 60 fans installed on one of the six peripheral walls of the chamber; the storm motion is accounted herein by setting the inclination of the IJ axis to non-normal angles. This latter technical expedient can reproduce the effect of cloud translation, meaning the downdraft-axis tilt at the ground, as first introduced by Byers and Braham (1948) and later confirmed by several authors (see, for instance, Fujita (1985)). This produces an asymmetric downburst outflow at the ground, with the intensification of the front-wind side and weakening of the rear-wind side, which was very clear also in our experiments.

The inclusion of ABL wind clearly affects the downburst field in a very different manner depending on whether the jet axis is vertical or inclined. As reported by Canepa et al. (2022a) in the case of vertical IJ, the entrainment of the ABL flow into the counter-directed primary vortex (PV) produces an intensification of the horizontal flow underneath the PV itself. However, this behavior is overall less evident for inclDBABL. The IJ-axis inclination, concordant with the direction of ABL, weakens the outflow and PV in the rear-wind side and, consequently, the entrainment of ABL wind reduces. At higher heights, the distribution of horizontal wind speeds is very similar between inclDB and inclDBABL, meaning that the outflow here is not influenced by the ABL-like flow. At the time of maximum intensity of the DB outflow, the height of maximum horizontal velocity drops drastically following the lowering of the surface layer underneath the PV. However, this height is higher at the interface between DB and ABL winds, due to the raising of PV above the surface after the entrainment of ABL air. The azimuth

angle $\alpha = 90^\circ$ is the least affected by both ABL flow and IJ-axis inclination and, hence, the pattern of maximum velocity height is similar among the different configurations. On the rear-wind side, the asymmetry and flow mixing caused by the DB-ABL interaction gives rise to wind speed vertical profiles rather dissimilar among different cases. At the front-wind side the profiles show a relative good match among each other. In all cases, the nose-like shape is well preserved.

The non-linearity of the superposition among flow components was proved mostly at the rear-wind side. Here, the embedment of ABL wind into the counter-directed PV structure intensifies the outflow velocities rather than producing an overall reduction. Instead, the linear combination gives higher outflow velocities at the front-wind side with respect to the actual measurements.

In agreement with the findings discussed by Canepa et al. (2022c, 2022a) and contrary to what was previously assumed in the literature, the turbulence intensity is found to be time-dependent. A sudden maximum occurs right before of that related to the horizontal velocity. This behavior is associated with the formation of the secondary vortex (SV) ahead of the downburst outflow and its interaction with the PV in the outer layer. The azimuth and radial locations of strong non-stationarity of turbulence seem to corroborate this hypothesis. The vertical profiles of turbulence intensity at the time of maximum velocity show rather high values and deviation among cases at the rear-wind side. Similar and lower values are observed in the front-wind region. Its maxima are observed at the lowest and highest heights of measurements, producing a C-like shape profile. While high values of I_V are expected at the top of the profile, following the wind speed reduction, those in the near-ground region are possibly due to the interaction between PV and SV. The turbulence intensity values along the elevation appear in good agreement with the previous experimental findings (Canepa et al., 2022a, 2022c, 2022a) and with full-scale vertical profile measurements (Canepa et al., 2020).

This study concludes the investigation of the vast experimental campaign on downburst winds performed at the WindEEE Dome in the context of the ERC Project THUNDERR (Solari et al., 2020). The analyses have returned a thorough and comprehensive picture of the physical behavior and dynamics of the downburst phenomenon. This can be extended to the full-scale environment thanks to the large Reynolds numbers involved in our experiments, $\mathrm{Re} > 10^6$, which allows us to consider the flow as "fully-turbulent" (Xu and Hangan, 2008) in analogy to the real scenario. This study lays the foundations for a clear understanding of the structural behavior to downburst winds. A crucial step in this sense will come from a comprehensive comparison of experimentally-produced and full-scale downburst outflows recorded within a large wind monitoring system installed in the Northern Mediterranean Sea (Canepa et al., 2020, 2023). This will eventually enable to build an analytical model to include in the design codes to evaluate the response of structures to thunderstorm winds.

Funding

The first and last authors acknowledge the support of the European Research Council (ERC) under the European Union's Horizon 2020 research and innovation program (grant agreement No. 741273) for the project THUNDERR—Detection, simulation, modelling and loading of thunderstorm outflows to design wind-safer and cost-efficient structures—awarded with an Advanced Grant 2016. Support from the Canada Foundation for Innovation (CFI) WindEEE Dome Grant (No. X2281B38) is also acknowledged.

Declaration of competing interest

The authors declare that they have no known competing financial interests or personal relationships that could have appeared to influence the work reported in this paper.

Acknowledgments

The authors are deeply grateful to Giovanni Solari for his essential contributions to the conceptualization, supervision, and funding of this research.

References

Abd-Elaal, E.-S., Mills, J.E., Ma, X., 2014. Empirical models for predicting unsteady-state downburst wind speeds. J. Wind Eng. Ind. Aerod. 129, 49–63. https://doi.org/10.1016/j.jweia.2014.03.011.

Allen, J.T., 2018. Climate change and severe thunderstorms. In: Oxford Research Encyclopedia of Climate Science. Oxford University Press. https://doi.org/10.1093/acrefore/9780190228620.013.62.

Asano, K., Iida, Y., Uematsu, Y., 2019. Laboratory study of wind loads on a low-rise building in a downburst using a moving pulsed jet simulator and their comparison with other types of simulators. J. Wind Eng. Ind. Aerod. 184, 313–320. https://doi.org/10.1016/j.jweia.2018.11.034.

Burlando, M., Romanić, D., Solari, G., Hangan, H., Zhang, S., 2017. Field data analysis and weather scenario of a downburst event in livorno, Italy, on 1 October 2012. Mon. Weather Rev. 145, 3507–3527. https://doi.org/10.1175/MWR-D-17-0018.1.

Burlando, M., Zhang, S., Solari, G., 2018. Monitoring, cataloguing, and weather scenarios of thunderstorm outflows in the northern Mediterranean. Nat. Hazards Earth Syst. Sci. 18, 2309–2330. https://doi.org/10.5194/nhess-18-2309-2018.

Byers, H.R., Braham, R.R., 1948. Thunderstorm structure and circulation. J. Meteorol. 5, 71–86. https://doi.org/10.1175/1520-0469(1948)005<0071:TSAC>2.0.CO;2.

Canepa, F., Burlando, M., Hangan, H., Romanic, D., 2022a. Experimental investigation of the near-surface flow dynamics in downburst-like impinging jets immersed in ABL-like winds. Atmosphere 13, 28. https://doi.org/10.3390/atmos13040621.

Canepa, F., Burlando, M., Romanic, D., Solari, G., Hangan, H., 2022b. Downburst-like experimental impinging jet measurements at the WindEEE Dome. Sci. Data 9, 243. https://doi.org/10.1038/s41597-022-01342-1.

Canepa, F., Burlando, M., Romanic, D., Solari, G., Hangan, H., 2022c. Experimental investigation of the near-surface flow dynamics in downburst-like impinging jets. Environ. Fluid Mech. https://doi.org/10.1007/s10652-022-09870-5.

Canepa, F., Burlando, M., Solari, G., 2020. Vertical profile characteristics of thunderstorm outflows. J. Wind Eng. Ind. Aerod. 206, 104332 https://doi.org/10.1016/j.jweia.2020.104332.

Canepa, F., Burlando, M., Repetto, M.P., 2023. Thunderstorm Outflows in the Mediterranean Sea Area [Data Set]. Zenodo. https://doi.org/10.5281/zenodo.7495115.

Chay, M.T., Albermani, F., Wilson, R., 2006. Numerical and analytical simulation of downburst wind loads. Eng. Struct. 28, 240–254. https://doi.org/10.1016/j.engstruct.2005.07.007.

Davenport, A.G., 1961. The application of statistical concepts to the wind loading of structures. Proc. Inst. Civ. Eng. 19, 449–472. https://doi.org/10.1680/iicep.1961.11304.

Fujita, T.T., 1985. The Downburst - Microburst and Macroburst - Report of Projects NIMROD and JAWS.

Fujita, T.T., 1983. Andrews AFB Microburst, vol. 205. SMRP Res. Pap., Chicago.

Fujita, T.T., 1981. Tornadoes and downbursts in the context of generalized planetary scales. J. Atmos. Sci. 38, 1511–1534.

Goff, R.C., 1976. Vertical structure of thunderstorm outflows. Mon. Weather Rev. 104.

Hadžiabdić, M., Hanjalić, K., 2008. Vortical structures and heat transfer in a round impinging jet. J. Fluid Mech. 596, 221–260. https://doi.org/10.1017/S002211200700955X.

Hangan, H., Refan, M., Jubayer, C., Romanic, D., Parvu, D., LoTufo, J., Costache, A., 2017. Novel techniques in wind engineering. J. Wind Eng. Ind. Aerod. 171, 12–33. https://doi.org/10.1016/j.jweia.2017.09.010.

Hjelmfelt, M.R., 1988. Structure and life cycle of microburst outflows observed in Colorado. J. Appl. Meteorol. 27, 900–927. https://doi.org/10.1175/1520-0450(1988)027<0900:SALCOM>2.0.CO;2.

Holmes, J.D., 1999. Modelling of extreme thunderstorm winds for wind loading of structures and risk assessment. In: Wind Engineering into the 21st Century. Presented at the Tenth International Conference on Wind Engineering, Balkema, Copenhagen, Denmark, 21-24 Jun. 1999, pp. 1409–1416.

Holmes, J.D., Hangan, H.M., Schroeder, J.L., Letchford, C.W., Orwig, K.D., 2008. A forensic study of the Lubbock-Reese downdraft of 2002. Wind Struct. 11, 137–152. https://doi.org/10.12989/WAS.2008.11.2.137.

Holmes, J.D., Oliver, S.E., 2000. An empirical model of a downburst. Eng. Struct. 22, 1167–1172. https://doi.org/10.1016/S0141-0296(99)00058-9.

Junayed, C., Jubayer, C., Parvu, D., Romanic, D., Hangan, H., 2019. Flow field dynamics of large-scale experimentally produced downburst flows. J. Wind Eng. Ind. Aerod. 188, 61–79. https://doi.org/10.1016/j.jweia.2019.02.008.

Kim, J., Hangan, H., 2007. Numerical simulations of impinging jets with application to downbursts. J. Wind Eng. Ind. Aerod. 95, 279–298. https://doi.org/10.1016/j.jweia.2006.07.002.

Letchford, C.W., Chay, M.T., 2002. Pressure distributions on a cube in a simulated thunderstorm downburst. Part B: moving downburst observations. J. Wind Eng. Ind. Aerod. 90, 733–753. https://doi.org/10.1016/S0167-6105(02)00163-0.

Lombardo, F.T., Smith, D.A., Schroeder, J.L., Mehta, K.C., 2014. Thunderstorm characteristics of importance to wind engineering. J. Wind Eng. Ind. Aerod. 125, 121–132. https://doi.org/10.1016/j.jweia.2013.12.004.

Mason, M., Wood, G., 2005. Influence of jet inclination on structural loading in an experimentally simulated microburst. In: Presented at the 6th Asia-Pacific Conference on Wind Engineering, South Korea, Seoul, p. 14.

Mason, M.S., Wood, G.S., Fletcher, D.F., 2009a. Numerical simulation of downburst winds. J. Wind Eng. Ind. Aerod. 97, 523–539. https://doi.org/10.1016/j.jweia.2009.07.010.

Mason, M.S., Wood, G.S., Fletcher, D.F., 2009b. Influence of tilt and surface roughness on the outflow wind field of an impinging jet. Wind Struct. 12, 179–204.

Moeini, M., Romanic, D., 2022. An analytical solution to the perturbation analysis of the interaction between downburst outflows and atmospheric boundary layer winds. J. Atmos. Sci. 1 https://doi.org/10.1175/JAS-D-22-0123.1.

Popiel, C.O., Trass, O., 1991. Visualization of a free and impinging round jet. Exp. Therm. Fluid Sci. 4 (3), 253–264. https://doi.org/10.1016/0894-1777(91)90043-Q.

Proctor, F.H., 1988. Case study of a low-reflectivity pulsating microburst: numerical simulation of the Denver, 8 July 1989, storm. J. Atmos. Sci. 45, 3137–3160.

Rädler, A.T., Groenemeijer, P.H., Faust, E., Sausen, R., Púčik, T., 2019. Frequency of severe thunderstorms across Europe expected to increase in the 21st century due to rising instability. Npj Clim. Atmospheric Sci. 2, 30. https://doi.org/10.1038/s41612-019-0083-7.

Romanic, D., Hangan, H., 2020. Experimental investigation of the interaction between near-surface atmospheric boundary layer winds and downburst outflows. J. Wind Eng. Ind. Aerod. 205, 104323 https://doi.org/10.1016/j.jweia.2020.104323.

Romanic, D., LoTufo, J., Hangan, H., 2019. Transient behavior in impinging jets in crossflow with application to downburst flows. J. Wind Eng. Ind. Aerod. 184, 209–227. https://doi.org/10.1016/j.jweia.2018.11.020.

Romanic, D., Nicolini, E., Hangan, H., Burlando, M., Solari, G., 2020. A novel approach to scaling experimentally produced downburst-like impinging jet outflows. J. Wind Eng. Ind. Aerod. 196, 104025 https://doi.org/10.1016/j.jweia.2019.104025.

Solari, G., Burlando, M., De Gaetano, P., Repetto, M.P., 2015. Characteristics of thunderstorms relevant to the wind loading of structures. Wind Struct. 20, 763–791. https://doi.org/10.12989/WAS.2015.20.6.763.

Solari, G., Burlando, M., Repetto, M.P., 2020. Detection, simulation, modelling and loading of thunderstorm outflows to design wind-safer and cost-efficient structures. J. Wind Eng. Ind. Aerod. 200, 104142 https://doi.org/10.1016/j.jweia.2020.104142.

Wu, Z., Iida, Y., Uematsu, Y., 2021. The flow fields generated by stationary and travelling downbursts and resultant wind load effects on transmission line structural system. J. Wind Eng. Ind. Aerod. 210, 104521 https://doi.org/10.1016/j.jweia.2021.104521.

Xu, Z., Hangan, H., 2008. Scale, boundary and inlet condition effects on impinging jets. J. Wind Eng. Ind. Aerod. 96, 2383–2402. https://doi.org/10.1016/j.jweia.2008.04.002.

Zhang, S., Solari, G., Burlando, M., Yang, Q., 2019. Directional decomposition and properties of thunderstorm outflows. J. Wind Eng. Ind. Aerod. 189, 71–90. https://doi.org/10.1016/j.jweia.2019.03.014.

Zhang, S., Solari, G., De Gaetano, P., Burlando, M., Repetto, M.P., 2018. A refined analysis of thunderstorm outflow characteristics relevant to the wind loading of structures. Probabilist. Eng. Mech. 54, 9–24. https://doi.org/10.1016/j.probengmech.2017.06.003.

Zhang, Y., Hu, H., Sarkar, P.P., 2013. Modeling of microburst outflows using impinging jet and cooling source approaches and their comparison. Eng. Struct. 56, 779–793. https://doi.org/10.1016/j.engstruct.2013.06.003.

Žužul, J., Ricci, A., Burlando, M., 2022. LES simulations of an experimentally-produced inclined downburst: implications of a storm motion. In: Proc. Of the 17th Conference on Wind Engineering (IN-VENTO 2022). Presented at the IN-VENTO 2022, Milan, Italy, 4-7 Sep. 2022.